PHYSICAL REVIEW B **111**, 184407 (2025)

Spontaneous anomalous Hall effect in two-dimensional altermagnets

Sajjan Sheoran and Pratibha Dev
Department of Physics and Astronomy, Howard University, Washington DC, USA

(Received 22 February 2025; revised 7 April 2025; accepted 24 April 2025; published 5 May 2025)

The anomalous Hall effect (AHE) is an efficient tool for detecting the Néel vector in collinear compensated magnets with spin-split bands, known as altermagnets (AMs). Here, we establish design principles for obtaining nonzero anomalous Hall conductivity in the recently proposed two-dimensional (2D) AMs using spin and magnetic group symmetry analysis. We show that only two of the seven nontrivial spin layer groups exhibit an unconventional in-plane AHE in which the Néel vector lies within the plane of the Hall current. Through first-principles simulations on bilayers of $\mathrm{MnPSe_3}$ and MnSe, we demonstrate the validity of our group theoretic framework for obtaining AHE with d- and i-wave altermagnetic orders, depending on the stacking of the bilayers. We find that the spin group symmetry is successful in determining the linear and cubic dependence of anomalous Hall conductivity in Néel vector space, although AHE is a relativistic effect. This work shows that the AHE in 2D AMs can probe the altermagnetic order and Néel vector reversal, thereby facilitating the miniaturization of altermagnetic spintronics.

DOI: 10.1103/PhysRevB.111.184407

I. INTRODUCTION

Altermagnetism (AM) has emerged as a novel class of collinear magnetism characterized by time-reversal symmetry (T) breaking in momentum space along with compensated magnetic order in real space [1–5]. Unlike conventional antiferromagnets (AFMs), where the opposite spin sublattices are connected by the inversion (P) and/or translation (τ) operations, in AMs they are connected by mirror-rotation symmetries. Hence, AMs show eV-scale nonrelativistic spin splittings [3], leading to highly spin-polarized currents, which are characteristic of ferromagnets (FMs). Since there is no net magnetization, AMs also show ultrafast switching dynamics and resilience towards stray fields, similar to that shown by AFMs [6–9]. This combination of properties of both FMs and AFMs in a single material makes AMs interesting not only for fundamental research, but also for spintronics-based applications by allowing for facile control and detection of spin states using different means, including electric or optical fields. Broken T-symmetry effects in AMs are experimentally detected through angle-resolved photoemission spectroscopy [10,11], spin-to-charge interconversion [12,13], and the anomalous Hall effect (AHE) [14]. To date, the experimental observation of altermagnetic effects is still limited to three-dimensional (3D) materials, i.e., MnTe [15], $\mathrm{Mn_5Si_3}$ [16], CrSb [17], and $\mathrm{RuO_2}$ [12].

The discovery of magnetic ordering in atomically thin materials opens up new possibilities for miniaturizing devices to the two-dimensional (2D) limit. However, achieving AM in 2D systems is difficult due to additional symmetry constraints. In 2D layers, the electronic bands are dispersionless along the out-of-plane direction [18–21]. As a result, in the 2D limit, the twofold rotation along the z axis (C_2^z) and horizontal mirror (M_z) symmetry transform $\boldsymbol{k} = (k_x, k_y)$ like P and τ, respectively. Therefore, for altermagnetism to emerge, the opposite spin sublattices must not be connected by M_z and/or C_2^z [19]. In spite of these exacting requirements, AM in 2D materials was predicted theoretically using a high-throughput computational approach ($\mathrm{RuF_4}$, $\mathrm{FeBr_3}$ [22,23]), bilayer stackings (CrSBr, $\mathrm{MnBi_2Te_4}$ [18,20]) and twisting bilayers [21,24,25]. The nonrelativistic understanding of 2D altermagnetism was recently established in Refs. [18–25]. However, unlike 3D bulk AMs, a comprehensive analysis of the magnetotransport effects (such as anomalous Hall and anomalous Nernst effects), and novel Néel vector detection methods for 2D AMs is still lacking.

Our work based on symmetry analysis and first-principles simulations elucidates the stringent symmetry requirement for observing AHE in the 2D AMs. We show an unconventional periodic dependence of AHE on the Néel-vector space, where the Néel vector lies in the plane of the Hall current. This is in contrast to the conventional FM-like Hall response, where Hall current is perpendicular to the magnetization [26,27]. By performing density functional theory (DFT) simulations on bilayers of $\mathrm{MnPSe_3}$ and MnSe, which are PT symmetric as monolayers, we achieved d- and i-wave altermagnetism with an in-plane anomalous Hall response as large as for the well-known bulk AMs—MnTe [15,28] and $\mathrm{Mn_5Si_3}$ [16,29]. Furthermore, we reveal the unique relationship of the AHE with the spin group symmetries and nonrelativistic spin-degenerate nodal lines. Moreover, the in-plane AHE is shown to be an efficient tool to probe the altermagnetic order and 180° Néel vector reversal in 2D AMs.

II. CALCULATION METHODS

DFT calculations have been carried out using the projector-augmented wave method [30], as implemented in the VASP package [31]. The Perdew-Burke-Ernzerhof (PBE) [32] functional within the generalized-gradient approximation, along with a Hubbard-U correction, are employed to accurately describe electronic interactions. Following Refs. [33,34], an effective U value of 3.0 eV was applied to the Mn-d orbitals using the approach of Dudarev *et al.* [35]. The Grimme-D3 scheme was used to account for the vdW interactions [36].

The AHE can be described by an order parameter called the Hall vector ($\boldsymbol{\sigma}_{\mathrm{H}}$), with the anomalous Hall current density given by $\boldsymbol{J} = \boldsymbol{\sigma}_{\mathrm{H}} \times \boldsymbol{E}$, where $\boldsymbol{E}$ is the electric field. The Hall vector is defined as: $\boldsymbol{\sigma}_{\mathrm{H}}$=($\sigma_{zy}$, σ_{xz}, σ_{yx}) [37], with $\sigma_{\alpha\beta}$ for $\alpha \neq \beta$ being the antisymmetric components of the conductivity tensor. At the microscopic level, the intrinsic contribution to anomalous Hall conductivity (AHC) is expressed as

$$\sigma_{\alpha\beta} = -\epsilon_{\alpha\beta\gamma}\frac{e^2}{\hbar}\int \frac{d\boldsymbol{k}}{(2\pi)^3}\sum_n f(\mathcal{E}_{n,\boldsymbol{k}})\Omega_\gamma(n,\boldsymbol{k}), \tag{1}$$

where $\epsilon_{\alpha\beta\gamma}$ is Levi-Civita symbol. $\mathcal{E}_{n,\boldsymbol{k}}$ and Ω_γ are the energy eigenvalue and Berry curvature, respectively, of the band with quantum number n. $f(\mathcal{E}_{n,\boldsymbol{k}})$ is the Fermi-Dirac distribution function. At zero temperature, the summation in Eq. (1) reduces to a sum over occupied bands. To simulate AHC within DFT, we constructed a tight-binding Hamiltonian from maximally localized Wannier functions, which were obtained through WANNIER90 [38]. Wannier interpolation of Berry curvature and AHC were postprocessed using the pruned FFT-based WANNIERBERRI [39] package. Note that rapid variations of Berry curvature are taken into account by integrating the Brillouin zone on a dense k mesh of 125 × 125 × 1 and with recursive adaptive mesh refinement. We conducted symmetry analysis using Ref. [40], FINDSYM [41], BILBAO crystallographic server [42], MAGNDATA [43], and AMCHECK [44].

III. RESULTS AND DISCUSSION

A. Symmetry analysis for AHE in 2D AMs

Since AMs display spin splitting of electronic structure without spin-orbit coupling (SOC), they are best characterized by spin group symmetries $[R_1||R_2]$, where R_1 and R_2 symmetry operations act on the decoupled spin and real space, respectively [3,45–47]. Just like in the case of AFMs, symmetry dictates a net zero magnetization in AMs. However, in AFMs, the spin-up and -down bands are degenerate. It is instructive to see which symmetries (in terms of spin group formalism) would result in a traditional AFM versus an AM. Collinear magnets, including AMs, always have spin-only symmetry $[\overline{C}_2||T]$, where $\overline{C}_2$ is a twofold rotation around the axis perpendicular to the collinear spins, followed by inversion in spin space [45]. The $[\overline{C}_2||T]$ transforms energy eigenstates as $[\overline{C}_2||T]E(s,\boldsymbol{k}) = E(s,-\boldsymbol{k})$, leading to even-parity spin splitting. The $[\overline{C}_2||T][C_2||P]$ and $[C_2||\tau]$ transform the energy eigenstates from $E(s,\boldsymbol{k})$ to $E(-s,\boldsymbol{k})$, which lead to spin degeneracy at an arbitrary k point. The C_2 operation is the twofold rotation about an axis perpendicular to collinear spins in spin space and, for simplicity, can be interpreted as spin space inversion. Additionally, for the 2D case ($k_z = 0$), the spin group symmetries $[C_2\|M_z]$ and $[C_2\|C_2^z]$ also lead to spin degeneracy (see Sec. I of Supplemental Material (SM) [48]). Overall, to obtain altermagnetism in 2D materials, opposite spin sublattices should not be connected by crystallographic P, τ, C_2^z, and M_z. However, there should exist at least one crystallographic symmetry connecting opposite spin sublattices to have symmetry-enforced net zero magnetization. The possible symmetry options are in-plane twofold rotation (i.e., $[C_2||C_2^x]$), vertical mirror plane (i.e., $[C_2||M_x]$), and out-of-plane fourfold rotation ($[C_2||C_4^z]$). The 2D AM case with $[C_2||M_x]$ symmetry is highlighted in Fig. 1.

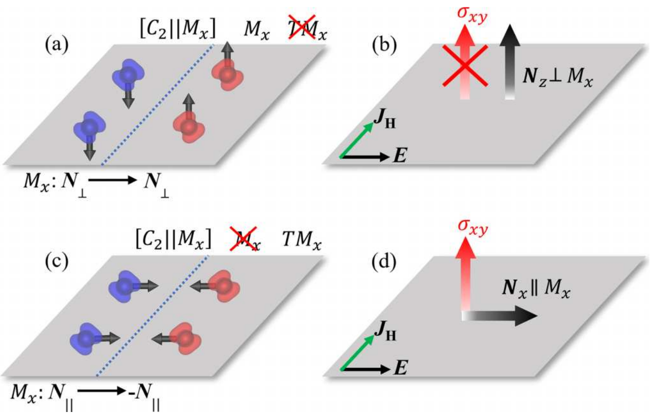

FIG. 1. Schematic diagram showing how symmetries determine the presence or absence of AHE in 2D altermagnets. In this example, the spin-group symmetry $[C_2||M_x]$ connects the opposite spin sublattices. (a) M_x symmetry is satisfied when the Néel vector ($\boldsymbol{N}$) is perpendicular to the direction of the mirror plane. Note that the direction of mirror plane refers to the direction normal to the mirror (here, x direction). (b) M_x symmetry forbids the AHE (see Table I). (c) $\boldsymbol{N}$ being parallel to the x direction violates the M_x symmetry and (d) thus the AHE is symmetry allowed. Since $\boldsymbol{N}$, $\boldsymbol{J}_{\mathrm{H}}$, and $\boldsymbol{E}$ all lie in the same plane (here, the x-y plane), this is referred to as the in-plane AHE.

The symmetry analysis for the relativistic AHE requires the considerations of magnetic symmetry operations acting on coupled spin and real spaces. From the symmetry perspective, the Hall vector, $\boldsymbol{\sigma}_{\mathrm{H}}$, transforms like a pseudovector, similar to magnetization. Therefore, the magnetic symmetry operations impose certain constraints on allowed components, σ_{ij}, of the system (see Table I and Sec. II of SM [48]). In particular, all components of the AHC tensor are symmetry forbidden if a material (2D or 3D) possesses either of the T, PT, $TC_{3,4,6}^{x,z}$, or $TS_{4,6}^{x,z}$ symmetries. Further constraints determining nonzero AHC are imposed by the 2D nature of the 2D AMs. As the Hall current is restricted to the plane of the 2D materials, the only component that is experimentally relevant is σ_{xy} (taking z as the out-of-plane axis). Hence, the presence of C_n^x, M_x, TM_z, and TC_2^z symmetries suppresses AHE in 2D materials as these symmetries result in zero σ_{xy} (see Table I). Overall, our symmetry analysis shows that three of the following conditions must be simultaneously satisfied to obtain a 2D AM with AHE: (i) absence of $[C_2||P]$, $[C_2||\tau]$, $[C_2||M_z]$, and $[C_2||C_2^z]$ spin group symmetries that will otherwise indicate that we have a conventional AFM, (ii) presence of at least one of $[C_2||C_2^x]$, $[C_2||M_x]$, and $[C_2||C_4^z]$ spin group symmetries, ensuring altermagnetism, and (iii) absence of T, PT, $TC_{3,4,6}^{x,z}$, $TS_{4,6}^{x,z}$, C_n^x, M_x, TM_z, and TC_2^z magnetic symmetries, which ensures nonzero σ_{xy}. These conditions for obtaining 2D AMs with AHE are partially related. For example, $[C_2||P]$ and PT occur simultaneously in collinear magnets. These conditions make observing AHE difficult in 2D AMs, and have largely remained unexplored.

TABLE I. Symmetry constraints on the components of the anomalous Hall conductivity tensor imposed by the magnetic point group operations. ✓ and ✗ denotes symmetry-allowed and -forbidden components, respectively. The z (x) denotes the out-of-plane (in-plane) direction.

	P	C_n^z	C_n^x	M_z	M_x	$S_{4,6}^z$	$S_{4,6}^x$	T	PT	TC_2^z	TC_2^x	TM_z	TM_x	$TC_{3,4,6}^{x,z}$	$TS_{4,6}^{x,z}$
σ_{xy}	✓	✓	✗	✓	✗	✓	✗	✗	✗	✗	✓	✗	✓	✗	✗
σ_{xz}	✓	✗	✗	✗	✗	✗	✗	✗	✗	✓	✓	✓	✓	✗	✗
σ_{yz}	✓	✗	✓	✗	✓	✗	✓	✗	✗	✓	✗	✓	✗	✗	✗

The magnetic symmetries depend on the Néel vector orientation with respect to the crystal symmetry. The Néel vector serves as an order parameter for AFMs and offers a robust nonvolatile approach to modifying magnetic symmetries [49]. Since, AMs also have net zero magnetization, the Néel vector could serve as a natural way to modify AHE. For example, consider the case of a 2D AM with $[C_2||M_x]$ symmetry, where opposite spin sublattices are connected through a vertical mirror plane (see Fig. 1). When the Néel vector is perpendicular to the x direction, the magnetic point group of the AM will contain M_x, leading to vanishing σ_{xy} [Figs. 1(a) and 1(b)]. However, aligning the Néel vector along the x direction will lead to the breaking of the M_x symmetry [Fig. 1(c)]. Hence, the presence of the Néel vector along the x direction will allow σ_{xy} [Fig. 1(d)]. It is worth mentioning that M_x and C_2^x impose the same condition on σ_{xy} (see Table I). Therefore, the presence of $[C_2||C_2^x]$ will allow (forbid) σ_{xy} when the Néel vector is parallel (perpendicular) to x direction. Following the same approach, we have classified the 2D AMs based on whether the AHE is allowed for the different Néel vector orientations, spin-momentum coupling and their nontrivial spin layer group (SLG) (see Table II and Sec. III of SM [48]). Interestingly, d-wave AMs with nontrivial SLG ${}^{2}2/{}^{2}m$ and i-wave AMs with nontrivial SLG ${}^{1}\overline{3}{}^{2}m$ allows for an in-plane AHE, where $\boldsymbol{N}$, $\boldsymbol{J}_{\mathrm{H}}$, and $\boldsymbol{E}$ lie in the x-y plane. Additionally, AMs with nontrivial SLGs ${}^{2}m{}^{2}m{}^{1}m$, ${}^{2}4/{}^{1}m$, ${}^{2}4/{}^{1}m{}^{2}m{}^{1}m$, ${}^{1}4/{}^{1}m{}^{2}m{}^{2}m$, and ${}^{1}6/{}^{1}m{}^{2}m{}^{2}m$ do not show an in-plane AHE due to the presence of TC_2^z symmetry. In accordance to symmetry analysis, σ_{xy} is always forbidden for 2D AMs when Néel vector points along the z direction.

B. Bilayer AMs as prototypical candidates

We exemplify the symmetry predictions of AHE in the 2D AMs using DFT simulations. For this, we chose the prototypical experimentally synthesized AFM materials, $\mathrm{MnPSe_3}$ [52–54] and MnSe [33,55–57] monolayers. In what follows, we provide detailed results for $\mathrm{MnPSe_3}$, while details of our calculations for MnSe are included in the Supplemental Material [48]. Both $\mathrm{MnPSe_3}$ and MnSe monolayers form a large class of 2D materials with G- and A-type AFM order, respectively, and a Néel transition temperature of ∼75 K [55,58]. The PT symmetry in $\mathrm{MnPSe_3}$ and MnSe monolayers enforces spin degeneracy and forbids the AHE effect (see Sec. IV of SM [48]). To obtain AM, we break PT symmetry of the monolayer $\mathrm{MnPSe_3}$ and MnSe by using the bilayer stacking approach [see Fig. 2(a)] [18]. We created different bilayer stacking by first taking the top layer to be the mirror reflection of the lower layer, followed by the translation of the upper layer in the basal plane (see also Sec. V of SM [48]). We have also used two different magnetic configurations with intralayer AFM, namely, $M\uparrow\downarrow\uparrow\downarrow$ and $M\uparrow\downarrow\downarrow\uparrow$ (the four arrows denote the magnetization directions of Mn atoms, with first two arrows being used for the lower layer and the last two arrows for the upper layer). DFT calculations were performed for potential energy surfaces of various high-symmetry stackings [see Fig. 2(b) for $\mathrm{MnPSe_3}$]. There are six degenerate lowest-energy configurations. These stackings are equivalent by symmetry and are obtained through translation of the upper layer by $\frac{1}{3}\boldsymbol{a}$, $\frac{1}{3}\boldsymbol{b}$, $\frac{2}{3}\boldsymbol{a}$, $\frac{2}{3}\boldsymbol{b}$, $\frac{1}{3}\boldsymbol{a}+\frac{1}{3}\boldsymbol{b}$, and $\frac{2}{3}\boldsymbol{a}+\frac{2}{3}\boldsymbol{b}$. Similarly, three high-energy stacking configurations, obtained through translation of the upper layer by $\boldsymbol{0}$, $\frac{1}{3}\boldsymbol{a}+\frac{2}{3}\boldsymbol{b}$, and $\frac{2}{3}\boldsymbol{a}+\frac{1}{3}\boldsymbol{b}$, are degenerate. Therefore, we take representative cases of bilayer $\mathrm{MnPSe_3}$ obtained through $\frac{1}{3}\boldsymbol{a}+\frac{1}{3}\boldsymbol{b}$ [see Fig. 2(c)] and $\frac{1}{3}\boldsymbol{a}+\frac{2}{3}\boldsymbol{b}$ [see Fig. 2(d)] and we name those

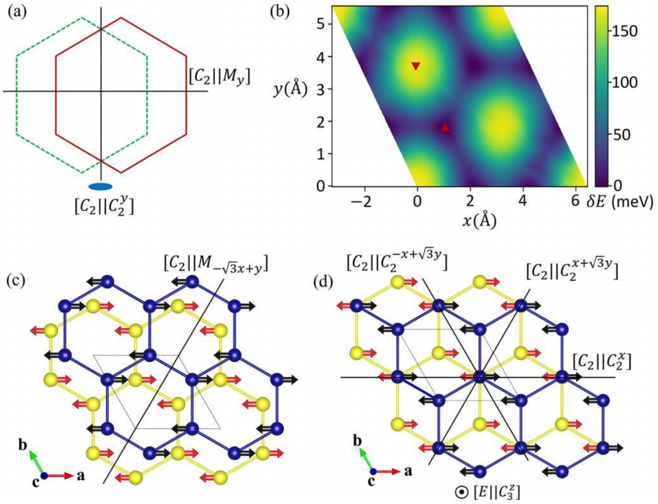

FIG. 2. Generation of AM through bilayer stackings. (a) The upper layer is obtained by taking the horizontal mirror reflection of the lower layer followed by in-plane translation. The bilayer stacking may have $[C_2||M_y]$ and $[C_2||C_2^y]$-like spin group symmetries depending on the shifting vector and the constituent monolayer. (b) The energy distribution of the bilayer $\mathrm{MnPSe_3}$ as a function of the shifting of the upper layer. (c) and (d) highlights the two high-symmetry stackings obtained by shifting the upper layer by $\frac{1}{3}\boldsymbol{a}+\frac{1}{3}\boldsymbol{b}$ (d-$\mathrm{MnPSe_3}$) and $\frac{1}{3}\boldsymbol{a}+\frac{2}{3}\boldsymbol{b}$ (i-$\mathrm{MnPSe_3}$), respectively, with representative Néel vector along x direction. The blue and yellow spheres denote the Mn atoms from the top and bottom layers, respectively. We have omitted the P and Se atoms for clear illustration (see Fig. S3 in the SM [48] for complete structure). The position of structures in (c) and (d) are also highlighted in potential energy surfaces in (b) with up- and down-triangle, respectively. The spin group symmetry operations are also indicated for each case.

stackings as d-MnPSe$_3$ and i-MnPSe$_3$, respectively. The rationale behind this unconventional nomenclature is elaborated in the following paragraph. The configurations $M \uparrow\downarrow\uparrow\downarrow$ and $M \uparrow\downarrow\downarrow\uparrow$ for d-MnPSe$_3$ are symmetrically equivalent. Since both magnetic configurations would exhibit similar anomalous Hall response, we chose to study AHE in $M \uparrow\downarrow\uparrow\downarrow$. On the other hand, for i-MnPSe$_3$, the two configurations, $M \uparrow\downarrow\downarrow\uparrow$ and $M \uparrow\downarrow\uparrow\downarrow$, are symmetrically inequivalent, with the former magnetic configuration being lower than $M \uparrow\downarrow\uparrow\downarrow$ by 0.22 meV. Since no symmetry operations connect opposite spin sublattices in the $M \uparrow\downarrow\uparrow\downarrow$ configuration of i-MnPSe$_3$, it is not altermagnetic. It is, instead, a Luttinger-compensated ferrimagnet [59–61] and therefore would exhibit FM-like Hall response (see Sec. V of SM [48] for details). Therefore, in order to study AHE in MnPSe$_3$ bilayers, we chose Néel orderings of $M \uparrow\downarrow\uparrow\downarrow$ and $M \uparrow\downarrow\downarrow\uparrow$ for d-MnPSe$_3$ and i-MnPSe$_3$, respectively [see Figs. 2(c) and 2(d)]. Although, i-MnPSe$_3$ bilayer stacking is metastable and higher in energy by 167 meV than the most stable d-MnPSe$_3$ stacking [Fig. 2(b)], studying i-MnPSe$_3$ is instructive not only for comparison with properties of d-MnPSe$_3$, but also as a stand in for other similar materials that exhibit AHE. For instance, twisted bilayers (tb) of hexagonal materials (such as tb-NiCl$_2$ [21], tb-MnBi$_2$Te$_4$ [24], and tb-MnPSe$_3$ [25]) have the same nonmagnetic/magnetic point group and altermagnetic order as of i-MnPSe$_3$ and are most sought-after candidates for AM in two dimensions. However, performing DFT+U+SOC simulations on twisted bilayers are computationally formidable task owing to supercell size.

We computed the electronic bands of d-MnPSe$_3$ and i-MnPSe$_3$ without SOC [see Figs. 3(a) and 3(b)]. The spin degeneracy in the energy bands can be explained through spin group symmetry operations [3]. The presence of $[C_2||O]$ symmetry leads to $[C_2||O]E(s,\boldsymbol{k}) = E(-s, O^{-1}\boldsymbol{k})$. Therefore, the bands are spin degenerate along the paths for which $O\boldsymbol{k} = \boldsymbol{k}$ or $O\boldsymbol{k} = \boldsymbol{k} + \boldsymbol{G}$, where $\boldsymbol{G}$ is a reciprocal lattice vector. For d-MnPSe$_3$, the spin-up and spin-down states are degenerate for the bands along the directions perpendicular and parallel to the mirror plane due to $[C_2||M_{-\sqrt{3}x+y}]$ and $[\overline{C}_2||T][C_2||M_{-\sqrt{3}x+y}]$, respectively (see Sec. VI of SM [48] for constant energy contours). AMs with two spin-degenerate nodal lines are classified as d-wave AMs, and d-MnPSe$_3$ belong to that class [3]. Similarly, the energy bands in i-MnPSe$_3$ are spin degenerate along all possible high-symmetry directions Γ-M, Γ-K, and M-K due to presence of three $[C_2||C_2^x]$-type spin group symmetries [Fig. 2(d)] and their combinations with spin-only symmetry $[\overline{C}_2||T]$. This results in the i-wave altermagnetism in the i-MnPSe$_3$. Note that although bands are nondegenerate at the general k point, the sum of spin splittings throughout the BZ, $\sum_{BZ} \mathcal{E}(s,\boldsymbol{k}) - \mathcal{E}(-s,\boldsymbol{k})$, is zero for each case [see Figs. 3(a) and 3(b)].

C. AHC and Néel vector relationship

We calculate the AHC, σ_{xy}, as a function of the Fermi energy for d-MnPSe$_3$ and i-MnPSe$_3$ for different Néel vector, $\boldsymbol{N}$, orientations [Figs. 3(c) and 3(d)]. The σ_{xy} shows a strong dependence on the $\boldsymbol{N}$ orientation and is absent when $\boldsymbol{N}$ is along the z direction. The anomalous Hall response is strongest for $\boldsymbol{N}$ along the x direction. The σ_{xy} for d-MnPSe$_3$ develops a strong peak of 202 S/cm around −0.23 eV, while σ_{xy} of i-MnPSe$_3$ develops a slightly weaker peak of 25 S/cm around −0.17 eV. Note that we observe a very sharp peak for i-MnPSe$_3$ around −0.25 eV and it may be difficult to achieve experimentally as it requires precise control of the Fermi energy. Interestingly, σ_{xy} is forbidden for $\boldsymbol{N}$ aligned along the y direction for i-MnPSe$_3$, while it shows an intermediate response for d-MnPSe$_3$. To understand this dependence of σ_{xy} on the Néel vector, we plot the anomalous Hall peaks for different $\boldsymbol{N}$ orientations in the x-y and x-z planes (see Fig. 4). For the x-y plane, the AHE is absent in d-MnPSe$_3$ for the Néel vector along 60°/240° due to the presence of the vertical mirror $M_{-\sqrt{3}x+y}$ [Fig. 4(a)]. Similarly, the AHE is absent for i-MnPSe$_3$ when $\boldsymbol{N}$ is perpendicular to any of the twofold rotation symmetries (30°, 90°, 150°, 210°, 270°, and 330°) [Fig. 4(c)]. When $\boldsymbol{N}$ points in the z direction, the AHE is forbidden due to presence of the $M_{-\sqrt{3}x+y}$ and C_2^x in d-MnPSe$_3$ and i-MnPSe$_3$, respectively [see Figs. 4(b) and 4(d)].

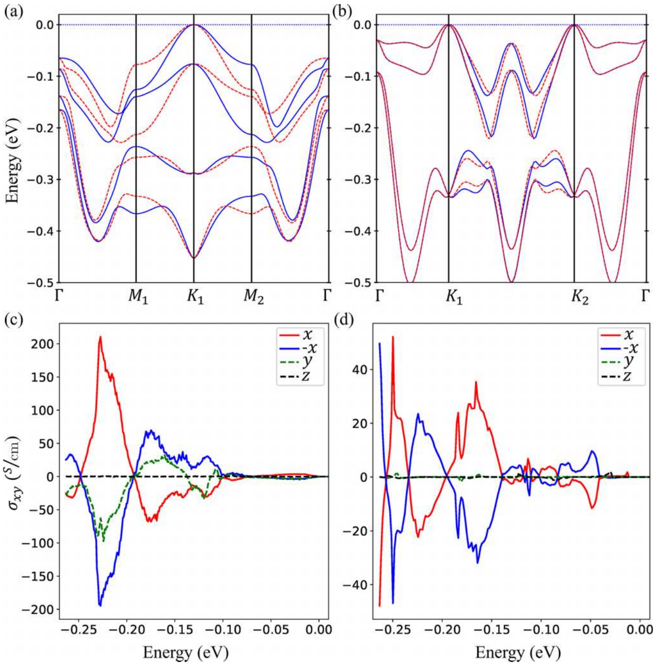

FIG. 3. Valence bands of (a) d-MnPSe$_3$ and (b) i-MnPSe$_3$ bilayer without inclusion of SOC. The red dashes and blue dots represent spin-up and spin-down bands, respectively. Anomalous Hall conductivity σ_{xy} of (c) d-MnPSe$_3$ and (d) i-MnPSe$_3$ as a function of Fermi energy for Néel vector pointing along different directions. The zero Fermi energy corresponds to valence band maximum.

Furthermore, we understand the periodicity by writing the general functional form of σ_{xy} as $\sigma_{xy}(\boldsymbol{N}) = \sum_{m,n,r} \lambda_{mnr} N_x^m N_y^n N_z^r$, where m, n, and r are whole numbers. Some components of λ_{mnr} are forbidden due to symmetries. For instance, $m+n+r$ is never even as it would violate the Onsager reciprocity relation: $\sigma_{xy}(\boldsymbol{N}) = \sigma_{yx}(-\boldsymbol{N})$ [62]. We use the method of invariants [63] $[O\sigma_{xy}(O\boldsymbol{N}) = \sigma_{xy}(\boldsymbol{N})]$ to obtain symmetry-allowed components λ_{mnr}. For this, we treat $\boldsymbol{N}$ as an extrinsic parameter instead of an intrinsic one [61,64]. Recall that $\boldsymbol{N}$ transforms like $\boldsymbol{N}' = \pm\mathrm{Det}(O)D(O)\boldsymbol{N}$, where $D(O)$ and $\mathrm{Det}(O)$ are the matrix representation and

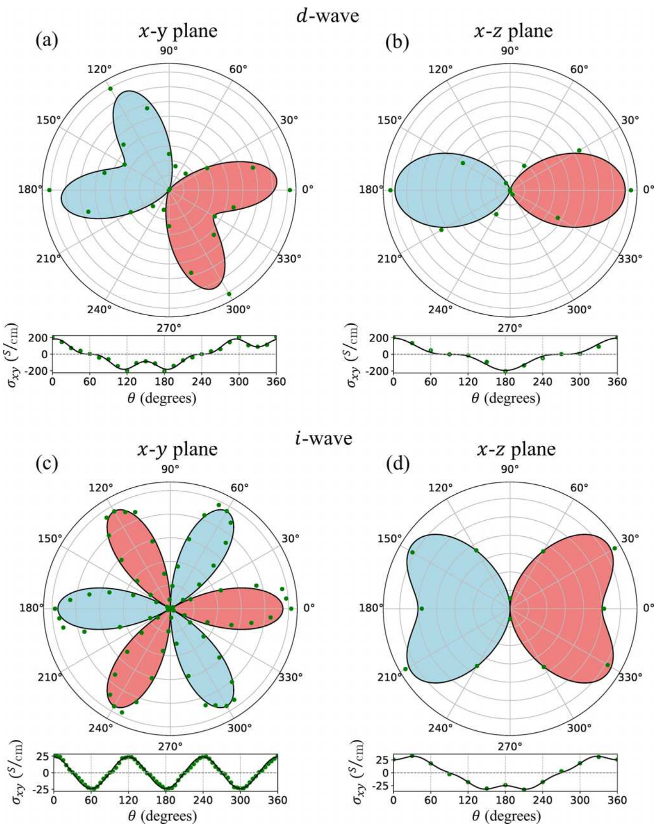

FIG. 4. The anomalous Hall conductivity (σ_{xy}) of d-MnPSe$_3$ with d-wave AM as a function of the Néel vector orientation in (a) x-y plane and (b) x-z plane at -0.23 eV. Similarly, (c) and (d) show the AHC for i-MnPSe$_3$ with i-wave AM at -0.17 eV. The regions with positive and negative σ_{xy} are highlighted with light red and light blue. The green dots represent the calculated DFT values while black curves are the fits using models in Eq. (2).

determinant of O. The $+$ $(-)$ sign is taken if O exchanges the same (opposite) spin sublattices [see Figs. 1(a) and 1(b)]. Table II summarizes the symmetry allowed profiles of $\sigma_{xy}(\boldsymbol{N})$ for 2D AMs with different spin group symmetry operations and nontrivial SLG (see also Sec. III of SM [48]). d-MnPSe$_3$ and i-MnPSe$_3$ have nontrivial SLG ${}^{2}2/{}^{2}m$ and ${}^{1}\overline{3}{}^{2}m$, respectively, and the σ_{xy}-$\boldsymbol{N}$ relationship can be expressed as

$$\begin{aligned}\sigma_{xy}^{{}^{2}2/{}^{2}m} &= \lambda_{100}N_x + \lambda_{300}N_x^3 + \lambda_{111}N_xN_yN_z + \lambda_{120}N_xN_y^2\\ &\quad + \lambda_{102}N_xN_z^2\\ \sigma_{xy}^{{}^{1}\overline{3}{}^{2}m} &= \lambda_{300}\left(N_x^3 - 3N_xN_y^2\right) + \lambda_{302}\left(N_x^3 - 3N_xN_y^2\right)N_z^2. \qquad (2)\end{aligned}$$

In Fig. 4, we fit the calculated DFT values of σ_{xy} with the models in Eq. (2). Note that for d-MnPSe$_3$ the mirror plane is $M_{-\sqrt{3}x+y}$ and not M_x. Therefore, we have rotated the models accordingly while fitting. The models provide good agreement with the DFT results. However, the fit shows slight deviations from the DFT results, which may be due to the structural distortions relative to the ideal symmetric configurations, and/or because we have ignored the higher-order terms in Eq. (2). Note that the σ_{xy} of d-MnPSe$_3$ depends on linear and cubic terms in the Néel vector $\boldsymbol{N}$ [Fig. 4(a)], while i-MnPSe$_3$ exhibits a purely cubic dependence on $\boldsymbol{N}$ [Fig. 4(c)]. Consequently, the strength of AHC in i-MnPSe$_3$ is smaller than that in d-MnPSe$_3$, with three AHC-forbidden directions in the x-y plane of the Néel vector space.

The dependence of σ_{xy} on $\boldsymbol{N}$ is derived for all 2D altermagnetic nontrivial SLGs in Table II. The AHE is forbidden for all g-wave 2D AMs due to the presence of $[E||C_4^z]$ symmetry, while the $[E||C_2^z, C_3^z]$ symmetries suppress the AHE in i-wave 2D AMs with the nontrivial SLG ${}^{1}6/{}^{1}m{}^{2}m{}^{2}m$. The presence of $[E||C_2^z]$, $[E||C_4^z]$, or $[C_2||C_4^z]$ leads to the presence of magnetic TC_2^z symmetry, which forbids the in-plane AHE. Most commonly, 2D magnets have an easy axis of magnetization that lies completely in-plane [34,57] or out-of-plane

TABLE II. AHE in 2D AMs with different nontrivial spin-layer group (SLG) symmetry. The superscripts 1 and 2 denote symmetry operations connecting atoms with the same and opposite spin magnetizations, respectively. Spin-momentum coupling is categorized based on the number of spin-degenerate nodal lines in the band dispersion. Specifically, d-, g-, and i-wave AMs exhibit 2, 4, and 6 spin-degenerate nodal lines passing through the Γ point, respectively, in the (k_x-k_y) momentum space. The nontrivial spin group symmetry operations are highlighted for each case. Note that the spin group operations $[E||E]$ and $[E||P]$ are excluded as they impose no restrictions on the AHC. Symmetry-invariant terms describe the functional dependence of the AHC σ_{xy} on the Néel vector components (N_x, N_y, N_z). The table also specifies whether σ_{xy} is allowed when the Néel vector is perpendicular or parallel to the out-of-plane direction (z). For forbidden cases, the relevant magnetic symmetry responsible is also indicated. Symmetry invariants up to cubic in N_i are included. Note that symmetry invariants may encompass higher-order terms, though their contributions are expected to be weak. Additionally, examples of well-known 2D AMs belonging to different SLGs are also tabulated. Entries marked with [⋆] denote examples from this work.

Nontrivial SLG	Spin-momentum coupling	Nontrivial spin group operations	Symmetry-allowed σ_{xy} terms	σ_{xy}		Examples
				$N \perp z$	$N\|\|z$	
${}^{2}2/{}^{2}m$	d-wave	$[C_2\|\|C_2^x]$	$N_x^{1,3}, N_xN_y^aN_z^b$ $(a+b=2)$	√	✗ (C_2^x)	RuF$_4$ [23], d-MnPSe$_3$ [⋆]
${}^{2}m{}^{2}m{}^{1}m$	d-wave	$[C_2\|\|C_2^x]$, $[E\|\|C_2^z]$	$N_xN_yN_z$	✗ (TC_2^z)	✗ (C_2^x)	MnTeMoO$_6$ [19]
${}^{2}4/{}^{1}m$	d-wave	$[C_2\|\|C_4^z]$, $[E\|\|C_2^z]$	$N_x^2N_z - N_y^2N_z, N_xN_yN_z$	✗ (TC_2^z)	✗ (C_2^x)	
${}^{2}4/{}^{1}m{}^{2}m{}^{1}m$	d-wave	$[C_2\|\|C_4^z]$, $[E\|\|C_2^z, C_2^x]$	$N_x^2N_z - N_y^2N_z$	✗ (TC_2^z)	✗ (C_2^x)	VSe$_2$O [50], CrO [51]
${}^{1}4/{}^{1}m{}^{2}m{}^{2}m$	g-wave	$[C_2\|\|C_2^x]$, $[E\|\|C_4^z, C_2^z]$	—	✗ (TC_2^z)	✗ (C_2^x)	VP$_2$H$_8$(NO$_4$)$_2$ [19]
${}^{1}\overline{3}{}^{2}m$	i-wave	$[C_2\|\|C_2^x]$, $[E\|\|C_3^z]$	$N_x^3 - 3N_xN_y^2$	√	✗ (C_2^x)	i-MnPSe$_3$ [⋆]
${}^{1}6/{}^{1}m{}^{2}m{}^{2}m$	i-wave	$[C_2\|\|C_2^x]$, $[E\|\|C_3^z, C_2^z]$	—	✗ (TC_2^z)	✗ (C_2^x)	

[65,66], and in such a scenario, the AHE can be observed for only ${}^{2}2/{}^{2}m$ and ${}^{1}\bar{3}{}^{2}m$ out of the seven nontrivial SLGs. Interestingly, the dependence of σ_{xy} on the Néel vector space is similar to that of the Berry curvature multipoles on k space [67] and the spin magnetization multipoles on real space [68].

The quantum origin of the large AHC lies in the SOC-induced avoided crossings, which act as opposite poles of Berry curvature (see Sec. VII of SM [48]). The highest σ_{xy} is achieved if the Fermi energy lies in the middle of the poles. In the case of the antiferromagnetic MnSe bilayer, with the translation of one layer relative to the other by $\frac{1}{3}\boldsymbol{a} + \frac{1}{3}\boldsymbol{b}$, we obtain effects similar to those in the d-MnPSe$_3$ bilayer, including altermagnetism (see Sec. VIII of SM [48]). Note that bilayer stacking of AFMs may also lead to weak ferromagnetism [69,70] where the opposite spin sublattices are not connected by any symmetry. For instance, the polar stacking of bilayer MnSe with basal plane translated by $\frac{1}{3}\boldsymbol{a} + \frac{2}{3}\boldsymbol{b}$ leads to weak ferromagnetism in the structure. In such cases, the anomalous Hall response is FM-like, where the AHE is also observed in the plane perpendicular to Néel vector. The weakly FM bilayer MnSe shows σ_{xy} when the Néel vector points along the z direction similar to conventional FMs [71,72] (see Sec. IX of SM [48]) and differ from the AHE in 2D AMs.

IV. SUMMARY

We have established the principles for obtaining the AHE in 2D AMs. Our analysis shows that TC_2^z and C_2^x are the most common magnetic point group symmetries that suppress the AHE in 2D AMs. Although the AHE is a relativistic effect, spin group symmetries are effective in explaining the unconventional periodicity in the in-plane anomalous Hall response, which can be used to detect the altermagnetic order and Néel vector reversal. We also show that the AHE is forbidden for the g-wave 2D AMs. Our symmetry predictions are supported by first-principles DFT simulations for bilayer MnPSe$_3$ with two different layer-stacking geometries used as prototypical candidates for the d- and i-wave AMs. Overall, 2D AMs are promising for the miniaturization of spintronic memory devices, with the Néel vector serving as the write-in mechanism and in-plane AHE for read off of the information. For the purpose of application in spintronics, 2D AMs that have an in-plane easy axis of magnetization will form a suitable choice. The spin-momentum coupling, and hence, the altermagnetic order can be controlled in twisted magnetic bilayers, depending on the symmetry of the constituent monolayers [24], providing an exceptional platform to achieve the AHE in experiments. Additionally, external parameters such as electric fields or strain may induce AHE in otherwise forbidden AMs [73–75]. We anticipate that the theoretical findings of this work will enrich the field of altermagnetic spintronics [4]. The approach provided here can be extended to other similar transverse effects, such as the anomalous Nernst effect [76] and the nonlinear Hall effect [77]. It should be pointed out that altermagnetic spin splittings are also known to generate unconventional spin Hall responses even without SOC [12,78]. A detailed analysis based on the spin group symmetry for 2D AMs, similar to our analysis for nonzero AHC, will be important for determining symmetry conditions that allow spin current generation in 2D AMs [79–81].

ACKNOWLEDGMENTS

This material is based upon work supported by the Air Force Office of Scientific Research under Award No. FA9550-23-1-0679 and the National Science Foundation Grant No. DMR-1752840. This work used the Expanse cluster at SDSC through allocation PHY180014 from the Advanced Cyberinfrastructure Coordination Ecosystem: Services & Support (ACCESS) program, which is supported by National Science Foundation Grants No. 2138259, No. 2138286, No. 2138307, No. 2137603, and No. 2138296.

DATA AVAILABILITY

The data that support the findings of this article are not publicly available. The data are available from the authors upon reasonable request.

---

[1] L.-D. Yuan, Z. Wang, J.-W. Luo, and A. Zunger, Prediction of low-Z collinear and noncollinear antiferromagnetic compounds having momentum-dependent spin splitting even without spin-orbit coupling, Phys. Rev. Mater. **5**, 014409 (2021).

[2] L.-D. Yuan, Z. Wang, J.-W. Luo, and A. Zunger, Strong influence of nonmagnetic ligands on the momentum-dependent spin splitting in antiferromagnets, Phys. Rev. B **103**, 224410 (2021).

[3] L. Šmejkal, J. Sinova, and T. Jungwirth, Beyond conventional ferromagnetism and antiferromagnetism: A phase with nonrelativistic spin and crystal rotation symmetry, Phys. Rev. X **12**, 031042 (2022).

[4] L. Šmejkal, J. Sinova, and T. Jungwirth, Emerging research landscape of altermagnetism, Phys. Rev. X **12**, 040501 (2022).

[5] S. Hayami, Y. Yanagi, and H. Kusunose, Bottom-up design of spin-split and reshaped electronic band structures in antiferromagnets without spin-orbit coupling: Procedure on the basis of augmented multipoles, Phys. Rev. B **102**, 144441 (2020).

[6] I. Žutić, J. Fabian, and S. D. Sarma, Spintronics: Fundamentals and applications, Rev. Mod. Phys. **76**, 323 (2004).

[7] E. Y. Tsymbal and I. Žutić, *Spintronics Handbook: Spin Transport and Magnetism: Volume Two: Semiconductor Spintronics* (CRC Press, Boca Raton, 2019).

[8] P. Němec, M. Fiebig, T. Kampfrath, and A. V. Kimel, Antiferromagnetic opto-spintronics, Nat. Phys. **14**, 229 (2018).

[9] J. Železný, P. Wadley, K. Olejník, A. Hoffmann, and H. Ohno, Spin transport and spin torque in antiferromagnetic devices, Nature Phys. **14**, 220 (2018).

[10] S. Lee, S. Lee, S. Jung, J. Jung, D. Kim, Y. Lee, B. Seok, J. Kim, B. G. Park, L. Šmejkal *et al.*, Broken Kramers degeneracy in altermagnetic MnTe, Phys. Rev. Lett. **132**, 036702 (2024).

[11] J. Krempaský, L. Šmejkal, S. W. D'souza, M. Hajlaoui, G. Springholz, K. Uhlířová, F. Alarab, P. C. Constantinou, V. Strocov, D. Usanov *et al.*, Altermagnetic lifting of Kramers spin degeneracy, Nature (London) **626**, 517 (2024).

[12] H. Bai, Y. C. Zhang, Y. J. Zhou, P. Chen, C. H. Wan, L. Han, W. X. Zhu, S. X. Liang, Y. C. Su, X. F. Han *et al.*, Efficient spin-to-charge conversion via altermagnetic spin splitting effect in antiferromagnet RuO_2, Phys. Rev. Lett. **130**, 216701 (2023).

[13] C.-T. Liao, Y.-C. Wang, Y.-C. Tien, S.-Y. Huang, and D. Qu, Separation of inverse altermagnetic spin-splitting effect from inverse spin Hall effect in RuO_2, Phys. Rev. Lett. **133**, 056701 (2024).

[14] L. Šmejkal, A. H. MacDonald, J. Sinova, S. Nakatsuji, and T. Jungwirth, Anomalous Hall antiferromagnets, Nature Rev. Mater. **7**, 482 (2022).

[15] R. Gonzalez Betancourt, J. Zubáč, R. Gonzalez-Hernandez, K. Geishendorf, Z. Šobáň, G. Springholz, K. Olejník, L. Šmejkal, J. Sinova, T. Jungwirth *et al.*, Spontaneous anomalous Hall effect arising from an unconventional compensated magnetic phase in a semiconductor, Phys. Rev. Lett. **130**, 036702 (2023).

[16] H. Reichlova, R. L. Seeger, R. González-Hernández, I. Kounta, R. Schlitz, D. Kriegner, P. Ritzinger, M. Lammel, M. Leiviskä, A. B. Hellenes *et al.*, Observation of a spontaneous anomalous Hall response in the Mn_5Si_3 d-wave altermagnet candidate, Nature Commun. **15**, 4961 (2024).

[17] S. Reimers, L. Odenbreit, L. Šmejkal, V. N. Strocov, P. Constantinou, A. B. Hellenes, R. J. Ubiergo, W. H. Campos, V. K. Bharadwaj, A. Chakraborty *et al.*, Direct observation of altermagnetic band splitting in CrSb thin films, Nature Commun. **15**, 2116 (2024).

[18] B. Pan, P. Zhou, P. Lyu, H. Xiao, X. Yang, and L. Sun, General stacking theory for altermagnetism in bilayer systems, Phys. Rev. Lett. **133**, 166701 (2024).

[19] S. Zeng and Y.-J. Zhao, Description of two-dimensional altermagnetism: Categorization using spin group theory, Phys. Rev. B **110**, 054406 (2024).

[20] S. Zeng and Y.-J. Zhao, Bilayer stacking a-type altermagnet: A general approach to generating two-dimensional altermagnetism, Phys. Rev. B **110**, 174410 (2024).

[21] R. He, D. Wang, N. Luo, J. Zeng, K.-Q. Chen, and L.-M. Tang, Nonrelativistic spin-momentum coupling in antiferromagnetic twisted bilayers, Phys. Rev. Lett. **130**, 046401 (2023).

[22] J. Sødequist and T. Olsen, Two-dimensional altermagnets from high throughput computational screening: Symmetry requirements, chiral magnons, and spin-orbit effects, Appl. Phys. Lett. **124**, 182409 (2024).

[23] M. Milivojević, M. Orozović, S. Picozzi, M. Gmitra, and S. Stavrić, Interplay of altermagnetism and weak ferromagnetism in two-dimensional RuF_4, 2D Mater. **11**, 035025 (2024).

[24] Y. Liu, J. Yu, and C.-C. Liu, Twisted magnetic van der Waals bilayers: An ideal platform for altermagnetism, Phys. Rev. Lett. **133**, 206702 (2024).

[25] S. Sheoran and S. Bhattacharya, Nonrelativistic spin splittings and altermagnetism in twisted bilayers of centrosymmetric antiferromagnets, Phys. Rev. Mater. **8**, L051401 (2024).

[26] S. Onoda, N. Sugimoto, and N. Nagaosa, Intrinsic versus extrinsic anomalous Hall effect in ferromagnets, Phys. Rev. Lett. **97**, 126602 (2006).

[27] R. Shindou and N. Nagaosa, Orbital ferromagnetism and anomalous Hall effect in antiferromagnets on the distorted fcc lattice, Phys. Rev. Lett. **87**, 116801 (2001).

[28] K. P. Kluczyk, K. Gas, M. J. Grzybowski, P. Skupiński, M. A, Borysiewicz, T. Fas, J. Suffczyński, J. Z. Domagala, K. Grasza, A. Mycielski *et al.*, Coexistence of anomalous Hall effect and weak magnetization in a nominally collinear antiferromagnet mnte, Phys. Rev. B **110**, 155201 (2024).

[29] M. Leiviskä, J. Rial, A. Bad'ura, R. L. Seeger, I. Kounta, S. Beckert, D. Kriegner, I. Joumard, E. Schmoranzerová, J. Sinova *et al.*, Anisotropy of the anomalous Hall effect in thin films of the altermagnet candidate Mn_5Si_3, Phys. Rev. B **109**, 224430 (2024).

[30] G. Kresse and D. Joubert, From ultrasoft pseudopotentials to the projector augmented-wave method, Phys. Rev. B **59**, 1758 (1999).

[31] G. Kresse and J. Furthmüller, Efficient iterative schemes for *ab initio* total-energy calculations using a plane-wave basis set, Phys. Rev. B **54**, 11169 (1996).

[32] J. P. Perdew, K. Burke, and M. Ernzerhof, Generalized gradient approximation made simple, Phys. Rev. Lett. **77**, 3865 (1996).

[33] K. Liu, X. Ma, S. Xu, Y. Li, and M. Zhao, Tunable sliding ferroelectricity and magnetoelectric coupling in two-dimensional multiferroic MnSe materials, npj Comput. Mater. **9**, 16 (2023).

[34] M. Rybak, P. E. Faria Junior, T. Woźniak, P. Scharoch, J. Fabian, and M. Birowska, Magneto-optical anisotropies of two-dimensional antiferromagnetic MPX_3 from first principles, Phys. Rev. B **109**, 054426 (2024).

[35] S. L. Dudarev, G. A. Botton, S. Y. Savrasov, C. J. Humphreys, and A. P. Sutton, Electron-energy-loss spectra and the structural stability of nickel oxide: An LSDA+U study, Phys. Rev. B **57**, 1505 (1998).

[36] S. Grimme, Semiempirical GGA-type density functional constructed with a long-range dispersion correction, J. Comput. Chem. **27**, 1787 (2006).

[37] N. Nagaosa, J. Sinova, S. Onoda, A. H. MacDonald, and N. P. Ong, Anomalous Hall effect, Rev. Mod. Phys. **82**, 1539 (2010).

[38] A. A. Mostofi, J. R. Yates, Y.-S. Lee, I. Souza, D. Vanderbilt, and N. Marzari, wannier90: A tool for obtaining maximally-localised Wannier functions, Comput. Phys. Commun. **178**, 685 (2008).

[39] S. S. Tsirkin, High performance Wannier interpolation of Berry curvature and related quantities with WannierBerri code, npj Comput. Mater. **7**, 33 (2021).

[40] M. S. Dresselhaus, G. Dresselhaus, and A. Jorio, *Group Theory: Application to the Physics of Condensed Matter* (Springer, Berlin, 2007).

[41] H. T. Stokes and D. M. Hatch, *FINDSYM:* Program for identifying the space-group symmetry of a crystal, J. Appl. Crystallogr. **38**, 237 (2005).

[42] M. I. Aroyo, J. M. Perez-Mato, C. Capillas, E. Kroumova, S. Ivantchev, G. Madariaga, A. Kirov, and H. Wondratschek, Bilbao crystallographic server: I. Databases and crystallographic computing programs, Zeitschrift für Kristallographie-Crystalline Materials **221**, 15 (2006).

[43] S. V. Gallego, J. M. Perez-Mato, L. Elcoro, E. S. Tasci, R. M. Hanson, K. Momma, M. I. Aroyo, and G. Madariaga, *MAGNDATA:* Towards a database of magnetic structures. I. The commensurate case, J. Appl. Crystallogr. **49**, 1750 (2016).

[44] A. Smolyanyuk, L. Šmejkal, and I. I. Mazin, A tool to check whether a symmetry-compensated collinear magnetic material is antiferro- or altermagnetic, SciPost Physics Codebases 30 (2024).

[45] D. B. Litvin and W. Opechowski, Spin groups, Physica **76**, 538 (1974).

[46] Y. Jiang, Z. Song, T. Zhu, Z. Fang, H. Weng, Z.-X. Liu, J. Yang, and C. Fang, Enumeration of spin-space groups: Toward a complete description of symmetries of magnetic orders, Phys. Rev. X **14**, 031039 (2024).

[47] P. Liu, J. Li, J. Han, X. Wan, and Q. Liu, Spin-group symmetry in magnetic materials with negligible spin-orbit coupling, Phys. Rev. X **12**, 021016 (2022).

[48] See Supplemental Material at http://link.aps.org/supplemental/10.1103/PhysRevB.111.184407 for further discussion on 2D altermagnetism, symmetry constraints on AHE, AHE−Néel vector relationship, monolayer and bilayer $MnPSe_3$ and MnSe, which includes Refs. [3,21,24,25,33,52–57,59–61,71,82–89].

[49] T. Jungwirth, X. Marti, P. Wadley, and J. Wunderlich, Antiferromagnetic spintronics, Nature Nanotechnol. **11**, 231 (2016).

[50] H.-Y. Ma, M. Hu, N. Li, J. Liu, W. Yao, J.-F. Jia, and J. Liu, Multifunctional antiferromagnetic materials with giant piezomagnetism and noncollinear spin current, Nature Commun. **12**, 2846 (2021).

[51] X. Chen, D. Wang, L. Li, and B. Sanyal, Giant spin-splitting and tunable spin-momentum locked transport in room temperature collinear antiferromagnetic semimetallic CrO monolayer, Appl. Phys. Lett. **123**, 022402 (2023).

[52] Z. Ni, A. Haglund, H. Wang, B. Xu, C. Bernhard, D. Mandrus, X. Qian, E. Mele, C. Kane, and L. Wu, Imaging the Néel vector switching in the monolayer antiferromagnet $MnPSe_3$ with strain-controlled Ising order, Nature Nanotechnol. **16**, 782 (2021).

[53] X. Li, X. Wu, and J. Yang, Half-metallicity in $MnPSe_3$ exfoliated nanosheet with carrier doping, J. Am. Chem. Soc. **136**, 11065 (2014).

[54] N. Sivadas, M. W. Daniels, R. H. Swendsen, S. Okamoto, and D. Xiao, Magnetic ground state of semiconducting transition-metal trichalcogenide monolayers, Phys. Rev. B **91**, 235425 (2015).

[55] M. Aapro, M. N. Huda, J. Karthikeyan, S. Kezilebieke, S. C. Ganguli, H. G. Herrero, X. Huang, P. Liljeroth, and H.-P. Komsa, Synthesis and properties of monolayer MnSe with unusual atomic structure and antiferromagnetic ordering, ACS Nano **15**, 13794 (2021).

[56] J. Wang, H. Zeng, W. Duan, and H. Huang, Intrinsic nonlinear Hall detection of the Néel vector for two-dimensional antiferromagnetic spintronics, Phys. Rev. Lett. **131**, 056401 (2023).

[57] S. Sheoran and S. Bhattacharya, Multiple Zeeman-type hidden spin splittings in PT-symmetric layered antiferromagnets, Phys. Rev. B **109**, L020404 (2024).

[58] X. Yi, Q. Chen, K. Wang, Y. Yu, Y. Yan, X. Jiang, C. Yan, and S. Wang, Exploring the interfacial coupling between graphene and the antiferromagnetic insulator $MnPSe_3$, Phys. Rev. B **108**, 125427 (2023).

[59] J. M. Luttinger and J. C. Ward, Ground-state energy of a many-fermion system. II, Phys. Rev. **118**, 1417 (1960).

[60] J. Luttinger, Fermi surface and some simple equilibrium properties of a system of interacting fermions, Phys. Rev. **119**, 1153 (1960).

[61] L.-D. Yuan, A. B. Georgescu, and J. M. Rondinelli, Nonrelativistic spin splitting at the Brillouin zone center in compensated magnets, Phys. Rev. Lett. **133**, 216701 (2024).

[62] L. D. Landau, J. S. Bell, M. Kearsley, L. Pitaevskii, E. Lifshitz, and J. Sykes, *Electrodynamics of Continuous Media* (Elsevier, Amsterdam, 2013), Vol. 8.

[63] L. C. L. Y. Voon and M. Willatzen, *The kp Method: Electronic Properties of Semiconductors* (Springer, Berlin, 2009).

[64] R.-C. Xiao, H. Li, H. Han, W. Gan, M. Yang, D.-F. Shao, S.-H. Zhang, Y. Gao, M. Tian, and J. Zhou, Anomalous-Hall Neel textures in altermagnetic materials, arXiv:2411.10147.

[65] J. Li, Y. Li, S. Du, Z. Wang, B.-L. Gu, S.-C. Zhang, K. He, W. Duan, and Y. Xu, Intrinsic magnetic topological insulators in van der Waals layered $MnBi_2Te_4$-family materials, Sci. Adv. **5**, eaaw5685 (2019).

[66] L. Webster and J.-A. Yan, Strain-tunable magnetic anisotropy in monolayer $CrCl_3$, $CrBr_3$, and CrI_3, Phys. Rev. B **98**, 144411 (2018).

[67] C.-P. Zhang, X.-J. Gao, Y.-M. Xie, H. C. Po, and K. T. Law, Higher-order nonlinear anomalous Hall effects induced by Berry curvature multipoles, Phys. Rev. B **107**, 115142 (2023).

[68] S. Bhowal and N. A. Spaldin, Ferroically ordered magnetic octupoles in d-wave altermagnets, Phys. Rev. X **14**, 011019 (2024).

[69] D. Jo, D. Go, Y. Mokrousov, P. M. Oppeneer, S.-W. Cheong, and H.-W. Lee, Weak ferromagnetism in altermagnets from alternating g-tensor anisotropy, arXiv:2410.17386.

[70] M. Roig, Y. Yu, R. C. Ekman, A. Kreisel, B. M. Andersen, and D. F. Agterberg, Quasi-symmetry constrained spin ferromagnetism in altermagnets, arXiv:2412.09338.

[71] T. Cao, D.-F. Shao, K. Huang, G. Gurung, and E. Y. Tsymbal, Switchable anomalous Hall effects in polar-stacked 2D antiferromagnet $MnBi_2Te_4$, Nano Lett. **23**, 3781 (2023).

[72] S. K. Chong, Y. Cheng, H. Man, S. H. Lee, Y. Wang, B. Dai, M. Tanabe, T.-H. Yang, Z. Mao, K. A. Moler *et al.*, Intrinsic exchange biased anomalous Hall effect in an uncompensated antiferromagnet $MnBi_2Te_4$, Nature Commun. **15**, 2881 (2024).

[73] M. Lejman, C. Paillard, V. Juvé, G. Vaudel, N. Guiblin, L. Bellaiche, M. Viret, V. E. Gusev, B. Dkhil, and P. Ruello, Magnetoelastic and magnetoelectric couplings across the antiferromagnetic transition in multiferroic $BiFeO_3$, Phys. Rev. B **99**, 104103 (2019).

[74] S. Sheoran, P. Bhumla, and S. Bhattacharya, Emergence of cubic ordered full-plane persistent spin textures in lead-free materials, Phys. Rev. Mater. **6**, 094602 (2022).

[75] S. Sheoran, M. Jain, R. Moulik, and S. Bhattacharya, Probing the uniaxial strain-dependent valley drift and Berry curvature in monolayer $MoSi_2N_4$, Phys. Rev. Mater. **7**, 114003 (2023).

[76] M. Mizuguchi and S. Nakatsuji, Energy-harvesting materials based on the anomalous Nernst effect, Sci. Tech. Adv. Mater. **20**, 262 (2019).

[77] Z. Du, H.-Z. Lu, and X. Xie, Nonlinear Hall effects, Nature Rev. Phys. **3**, 744 (2021).

[78] R. González-Hernández, L. Šmejkal, K. Výborný, Y. Yahagi, J. Sinova, T. Jungwirth, and J. Železný, Efficient electrical spin splitter based on nonrelativistic collinear antiferromagnetism, Phys. Rev. Lett. **126**, 127701 (2021).

[79] W. Yan, O. Txoperena, R. Llopis, H. Dery, L. E. Hueso, and F. Casanova, A two-dimensional spin field-effect switch, Nature Commun. **7**, 13372 (2016).

[80] W. Han, R. K. Kawakami, M. Gmitra, and J. Fabian, Graphene spintronics, Nature Nanotechnol. **9**, 794 (2014).

[81] D. J. de Sousa, M. J. Sammon, R. Kim, H. Li, I. A. Young, and T. Low, Spin torque generated by valley Hall effect in WSe_2, Phys. Rev. B **106**, 184412 (2022).

[82] C. Wang, Y. Gao, and D. Xiao, Intrinsic nonlinear Hall effect in antiferromagnetic tetragonal CuMnAs, Phys. Rev. Lett. **127**, 277201 (2021).

[83] N. Sivadas, S. Okamoto, and D. Xiao, Gate-controllable magneto-optic Kerr effect in layered collinear antiferromagnets, Phys. Rev. Lett. **117**, 267203 (2016).

[84] U. Herath, P. Tavadze, X. He, E. Bousquet, S. Singh, F. Muñoz, and A. H. Romero, PyProcar: A Python library for electronic structure pre/post-processing, Comput. Phys. Commun. **251**, 107080 (2020).

[85] S. Singh and A. C. Garcia-Castro, Kagome KMn_3Sb_5 metal: Magnetism, lattice dynamics, and anomalous Hall conductivity, Phys. Rev. B **108**, 245143 (2023).

[86] H. Chen, Q. Niu, and A. H. MacDonald, Anomalous Hall effect arising from noncollinear antiferromagnetism, Phys. Rev. Lett. **112**, 017205 (2014).

[87] L. Šmejkal, R. González-Hernández, T. Jungwirth, and J. Sinova, Crystal time-reversal symmetry breaking and spontaneous Hall effect in collinear antiferromagnets, Sci. Adv. **6**, eaaz8809 (2020).

[88] R. Peng, T. Zhang, Z. He, Q. Wu, Y. Dai, B. Huang, and Y. Ma, Intrinsic layer-polarized anomalous Hall effect in bilayer $MnBi_2Te_4$, Phys. Rev. B **107**, 085411 (2023).

[89] A. Gao, Y.-F. Liu, C. Hu, J.-X. Qiu, C. Tzschaschel, B. Ghosh, S.-C. Ho, D. Bérubé, R. Chen, H. Sun *et al.*, Layer Hall effect in a 2D topological axion antiferromagnet, Nature (London) **595**, 521 (2021).